Research paper

An integrated workflow for stress and flow modelling using outcrop-derived discrete fracture networks

K. Bisdom[a,*], H.M. Nick[a,b], G. Bertotti[a]

[a] Department of Geoscience & Engineering, Delft University of Technology, Delft, Netherlands
[b] The Danish Hydrocarbon Research and Technology Centre, Technical University of Denmark, Copenhagen, Denmark

ARTICLE INFO

ABSTRACT

Fluid flow in naturally fractured reservoirs is often controlled by subseismic-scale fracture networks. Although the fracture network can be partly sampled in the direct vicinity of wells, the inter-well scale network is poorly constrained in fractured reservoir models. Outcrop analogues can provide data for populating domains of the reservoir model where no direct measurements are available. However, extracting relevant statistics from large outcrops representative of inter-well scale fracture networks remains challenging. Recent advances in outcrop imaging provide high-resolution datasets that can cover areas of several hundred by several hundred meters, i.e. the domain between adjacent wells, but even then, data from the high-resolution models is often upscaled to reservoir flow grids, resulting in loss of accuracy. We present a workflow that uses photorealistic georeferenced outcrop models to construct geomechanical and fluid flow models containing thousands of discrete fractures covering sufficiently large areas, that does not require upscaling to model permeability. This workflow seamlessly integrates geomechanical Finite Element models with flow models that take into account stress-sensitive fracture permeability and matrix flow to determine the full permeability tensor. The applicability of this workflow is illustrated using an outcropping carbonate pavement in the Potiguar basin in Brazil, from which 1082 fractures are digitised. The permeability tensor for a range of matrix permeabilities shows that conventional upscaling to effective grid properties leads to potential underestimation of the true permeability and the orientation of principal permeabilities. The presented workflow yields the full permeability tensor model of discrete fracture networks with stress-induced apertures, instead of relying on effective properties as most conventional flow models do.

1. Introduction

Natural fracture networks are multiscale systems that develop through a combination of mechanisms that are only partly understood (Olson et al., 2009; Philip et al., 2005). Understanding the multiscale distribution of fracture networks in the subsurface allows for optimisation of fractured reservoir development (Nelson, 2001). However, limited observations from seismic and wells do not provide the complete fracture network geometry and associated flow properties, particularly of the subseismic fracture network (Fabuel-Perez et al., 2010; Martinez-Landa et al., 2016). Outcrops are the only source that provides realistic descriptions of fracture networks, as no models exist that can create realistic fracture networks on the scale of fractured reservoirs. To derive lessons for fractured reservoirs, we need outcropping datasets that contain at least several hundred fractures covering several orders of magnitude in spacing and length, without suffering from censoring and truncation artefacts, over an area that covers at least several grid blocks in conventional reservoir flow models (Bonnet et al., 2001; Ortega et al., 2006). Such datasets are not easily obtained from conventional outcrop photographs or scanline studies, as these methods capture only a limited number of scales (Bisdom et al., 2014).

Photogrammetry, particularly Structure from Motion (SfM) Multiview stereo (MVS), is an inexpensive and fast method to accurately map 3-D structures from 2-D images taken from different positions (Harwin and Lucieer, 2012; Ullman, 1979). In recent years, this method has been embraced by geologists to create digital outcrop models as an alternative to the more expensive and less flexible LiDAR (Light Image Detection And Ranging) methods (Hodgetts, 2013; Mahmud et al., 2015; Reif et al., 2011; Rotevatn et al., 2009; Tavani et al., 2014; Wilson et al., 2011). Partly overlapping images are aligned by identifying and extracting common points, which can be positioned in 3-D space to reconstruct the outcrop geometry (Bemis et al., 2014; James and Robson, 2012). The resulting models provide a complete

---

* Corresponding author.
  E-mail address: kevin.bisdom@gmail.com (K. Bisdom).

and unobstructed viewpoint of the outcrop that can be changed and adjusted for any purpose (Tavani et al., 2016).

As this approach requires that the outcrop is fully covered by images with an overlap of at least 50%, Unmanned Aerial Vehicles (UAVs or drones), equipped with a camera and positioning sensors, are best suited to acquire the images required for photogrammetry modelling (e.g. Bemis et al., 2014; Bond et al., 2015; Hodgetts, 2013; James and Robson, 2012; Tavani et al., 2014; Vasuki et al., 2014; Vollgger and Cruden, 2016). Fracture geometries can be extracted from the resulting georeferenced models in 2-D or 3-D (Duelis Viana et al., 2016; Hardebol and Bertotti, 2013; Tavani et al., 2014). Extraction of 2-D data from a 3-D photogrammetry model is more accurate than fracture interpretation from conventional 2-D images, as the photogrammetry model is accurately orthorectified and the multiple viewpoints allow for more precise digitisation of fracture geometry. Irrespective of whether the fracture data is used for 2-D or 3-D analysis, 3-D outcrop models provide a higher accuracy.

The second challenge is to obtain realistic aperture predictions from outcropping geometries. At depth, permeability is a function of aperture, which is partly controlled by the in-situ stresses (Baghbanan and Jing, 2008; Lei et al., 2015; Tao et al., 2009; Zoback, 2007), but pressure relief during exhumation and weathering dissolves cements and changes aperture. Outcropping apertures are therefore not representative, unless it can be proven that fractures have not been reactivated during exhumation. This is typically assumed to be the case for veins (e.g. Hooker et al., 2014), but preserved veins are relatively rare. Alternatively, aperture is modelled as a function of stress, using subcritical crack growth as defined by Linear Elastic Fracture Mechanics (LEFM) or conductive shearing defined by Barton-Bandis (Barton, 1982; Barton et al., 1985; Barton and Bandis, 1980; Lawn and Wilshaw, 1975; Olson, 2003; Pollard and Segall, 1987; Vermilye and Scholz, 1995). These models require the local stress state, which is typically derived from Finite Element (FE) models with explicit fracture representations (Barton, 2014; Bisdom et al., 2016b; Lei et al., 2016, 2014; Nick et al., 2011).

The third challenge is modelling permeability through fractured rocks, taking into account the coupled flow through fractures and matrix (Belayneh et al., 2009; Geiger et al., 2013; Lang et al., 2014). Conventional reservoir simulation tools scale up fracture density, porosity and permeability to effective grid properties in dual-porosity dual-permeability grids, resulting in a significantly simplified flow model (Cottereau et al., 2010; Geiger and Matthäi, 2012; Jonoud and Jackson, 2008). Methods exist to model flow through discrete fracture-matrix models without requiring upscaling, making use of a Finite-Element Finite-Volume (FE-FV) approach, but the use of these methods is often limited to relatively small-scale synthetic fracture networks (Lei et al., 2014; Matthäi and Belayneh, 2004).

These individual problems have been studied extensively, focusing on 3-D outcrop modelling (Hodgetts, 2013; Tavani et al., 2014; Vasuki et al., 2014), meshing (Karimi-Fard and Durlofsky, 2016; Nejati et al., 2016; Nick and Matthäi, 2011a; Paluszny et al., 2007) and flow modelling (Lang et al., 2014; Nick and Matthäi, 2011b), but integrating these components remains a challenge. Our aim is to present an integrated workflow for modelling the complete permeability tensor of large-scale fracture networks with apertures representative of in-situ stress conditions by combining fast data acquisition using a UAV with outcrop modelling using photogrammetry (Fig. 1). This workflow builds upon the stress-aperture modelling approach presented in Bisdom et al. (2016b), making use of the geometrical aperture approximation from Bisdom et al. (2016d), and the modelling of permeability for a range of aperture definitions presented in Bisdom et al. (2016d). The 3-D outcrop models are used to accurately digitise fracture patterns in 2-D, which form the basis for stress, aperture and equivalent permeability (i.e. combined matrix and fracture permeability) models. The main result is a discrete fracture-matrix model consisting of an unstructured mesh with discrete fractures, from which

the full permeability tensor is calculated. The aim of this workflow is to improve the representativeness of outcrops as a proxy for flow in naturally fractured reservoirs, by capturing larger-scale high-resolution fracture patterns covering distances comparable to well spacing in fractured reservoirs, followed by modelling of aperture and flow representative of subsurface conditions. We illustrate the effectiveness of the workflow using an example of 2-D fracture patterns in outcropping carbonates in the Potiguar Basin, NE Brazil (Bisdom et al., 2017; de Graaf et al., 2017).

2. Quantitative outcrop modelling using a UAV and photogrammetry

2.1. Image acquisition with a UAV

We use a multi-rotor UAV (Fig. 2) to acquire images of multiscale fracture patterns over an area that covers several reservoir simulation grid blocks, which are subsequently merged into 2-D georeferenced outcrop models. To ensure that an area is fully covered by images with constant overlap, flight paths are programmed prior to flights (Fig. 3). The programmed flights are automatically executed and controlled using a GNSS sensor (2 m accuracy) for horizontal positioning and a temperature-compensated barometer (dm-accuracy) for vertical positioning. A magnetic compass provides the absolute heading and accelerometers and a gyroscope further control the position of the UAV and ensure stable operation. Flight and environment conditions are continuously monitored and stored during flights for quality-check and diagnostic purposes.

Outcrop images are taken with a 14-megapixel compact camera in a motorised mount attached to the UAV. The resulting image resolution depends on the altitude and camera specifications. A distance of 50 m between the UAV and the surface of interest yields a resolution R of 1.44 cm/px, which changes linearly with distance H (in m):

$$R = \frac{100 w_s H}{w_i F_r},\tag{1.1}$$

where w_s is the camera sensor width (in mm), w_i is the image width (in pixels) and F_r is the real focal length (in mm) for the focal length in a 35 mm equivalent ($F35$):

$$F_r = \frac{F_{35} w_s}{34.6}.\tag{1.2}$$

Depending on outcrop size and required resolution, most flights are between 20 and 100 m altitude, corresponding to resolutions of 0.6–2.9 cm/px respectively. For each image, the corresponding UAV position (horizontal coordinates and altitude) and orientation are determined using the GNSS sensor and barometer. To further constrain the outcrop position, brightly marked GCPs (Ground Control Points) are positioned on the outcrop surface, which are georeferenced with a GPS, and we measure the distance between these points using a hand-held laser range finder for further scaling of the model.

2.2. Outcrop model construction using photogrammetry

Using Agisoft PhotoScan®, we process the UAV images and location data into georeferenced 2-D and 3-D outcrop models. This workflow consists of image alignment, point cloud generation, surface meshing and texturing (Fig. 4 and Fig. 5).

2.2.1. Image alignment

The approximate position from where each image is taken, is used to identify the image pairs that are likely to overlap. Common points are identified, extracted and positioned in 3-D in a *sparse point cloud* (Fig. 4a). The vertical position of a point is determined from the relative change in position in the partly overlapping images, where one point is imaged from different angles.
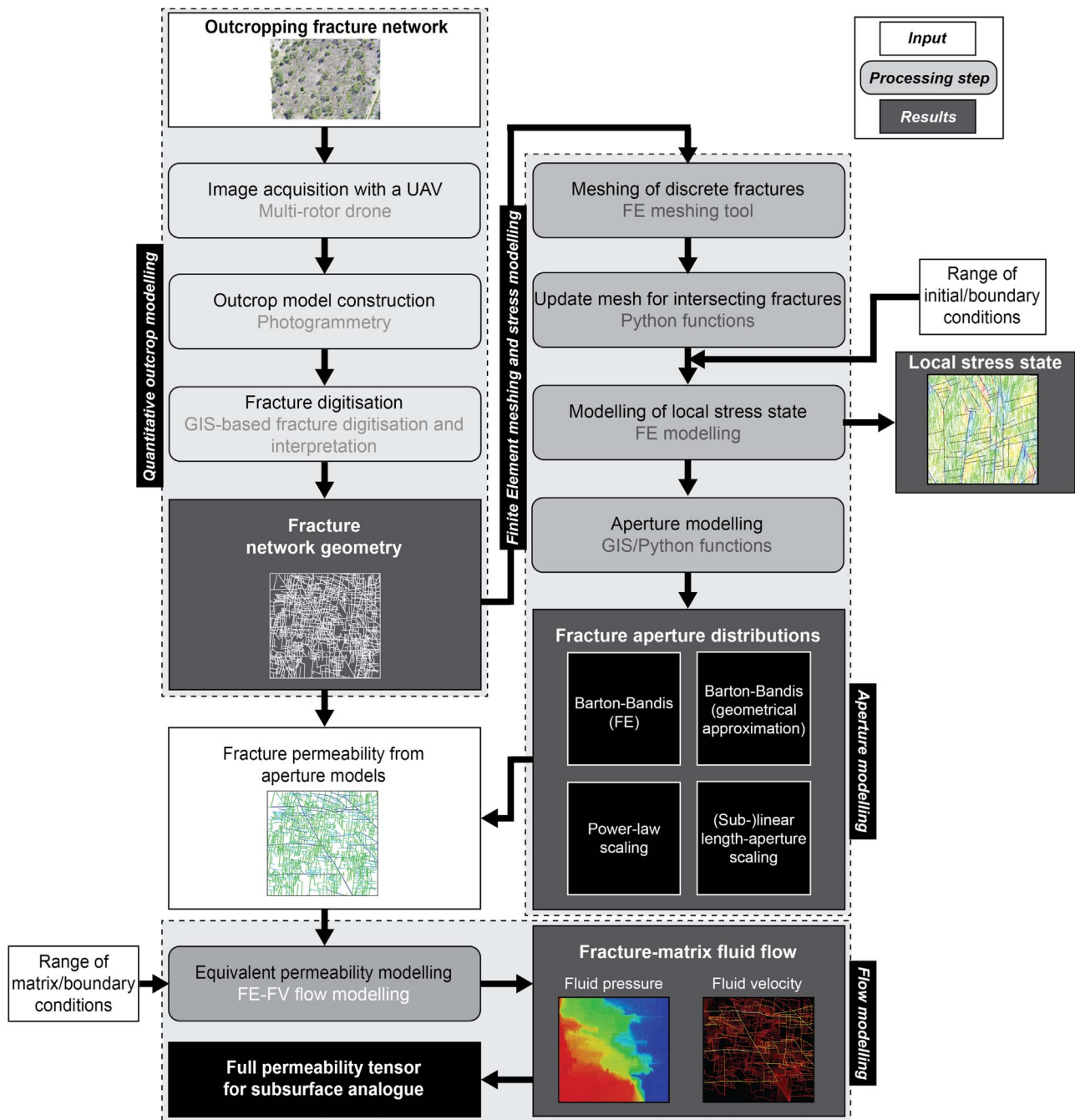
Fig. 1. Workflow for obtaining flow-based principal permeability from outcropping fracture networks that are representative of subsurface reservoir stress and pressure conditions, by taking into account the impact of stress on aperture and flow. See Appendix A for details on the aperture models.

2.2.2. Point cloud generation

Once images are aligned, all points from the aligned images are extracted and positioned in 3-D to generate a *dense point cloud* (Fig. 4b and Fig. 5a). Depending on flight altitude, the point cloud can have a resolution that is similar to LiDAR datasets. A single flight at 50 m altitude, capturing 100 images covering an area of 200 m×200 m, results in a dense point cloud of $1.4×10^7$ points (35 points per m²; Fig. 4b). Higher-detail models, for example captured from an altitude of 3 m, yield point clouds of $8.6×10^7$ points for an area of 20 m×30 m ($1.4×10^4$ points per m²; Fig. 5a).

When the images are georeferenced, aligning and dense point cloud generation are relatively fast processes that can be completed during a fieldwork campaign, providing an almost immediate data check to analyse whether data acquisition was successful or additional flights

are required. Furthermore, having already a high-resolution point cloud in the field can be useful in identifying interesting features or sections of the outcrop that warrant further inspection, or additional higher-resolution flights.

2.2.3. Surface generation

Interpretation of outcropping features requires converting the point cloud into a meshed surface consisting of triangulated elements (Fig. 5). The meshed surface can have the same resolution as the dense point cloud, but for sub-horizontal pavements a downsampled mesh is typically sufficient. For this example, the point cloud consists of $8.6×10^7$ points whereas the resulting surface is downsampled to $2×10^6$ elements (Fig. 5b,c). This surface has a sufficiently high resolution for
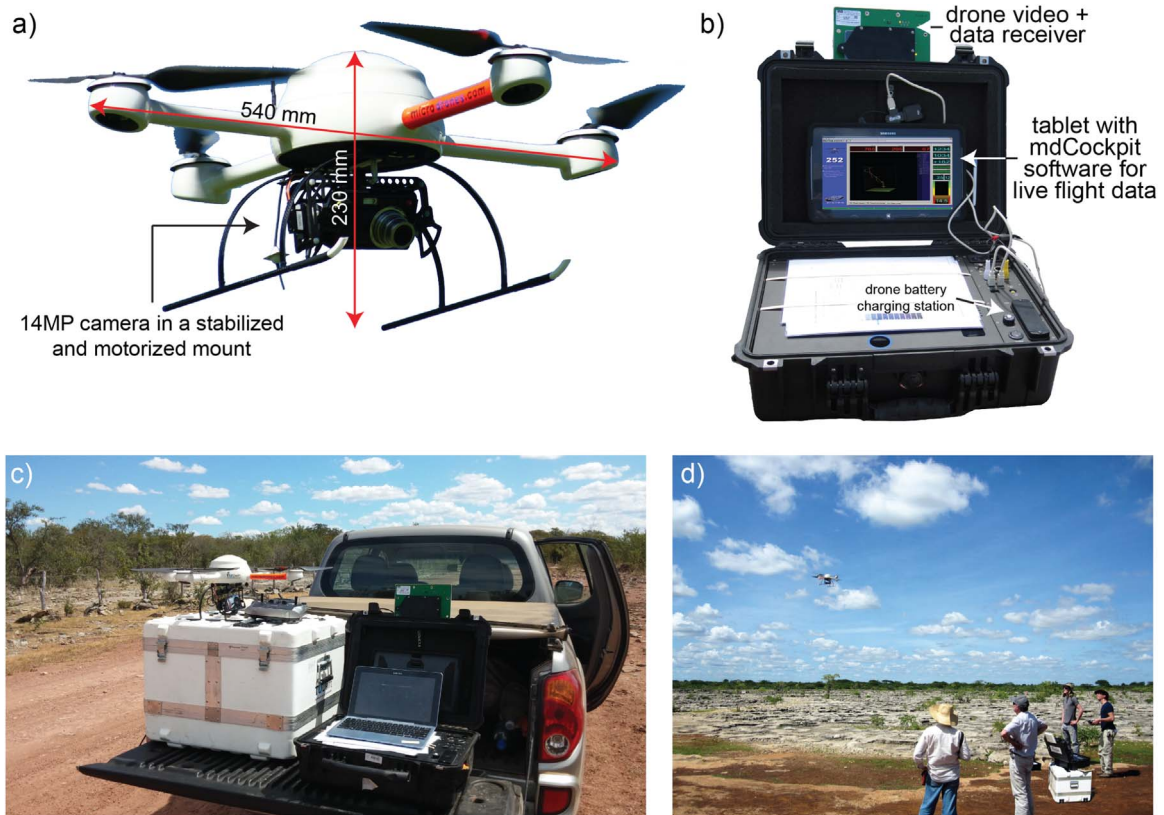
Fig. 2. Overview of the UAV equipment in the field: a) UAV (microdrones md4-200) with compact camera; b) Base station with receivers and tablet to receive and store flight data and video; c) Preparation for UAV deployment in the field. White case is the UAV transport case; d) Use of the UAV to image carbonate pavements.
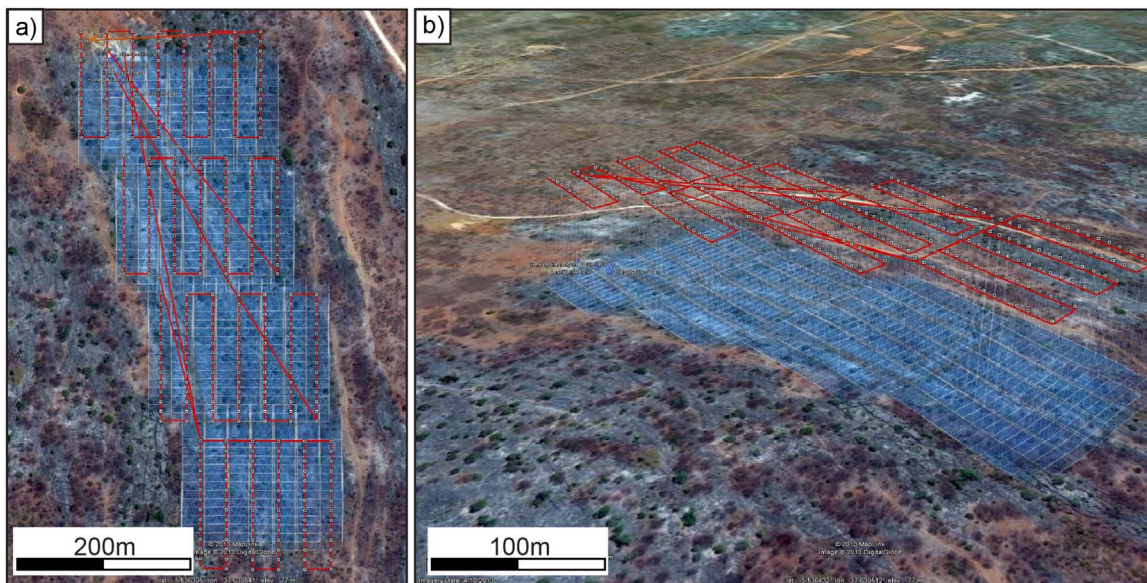

Fig. 3. Programming and visualising GNSS-steered flights: a) Top view of flight path (red) and imaged area (blue) in Google Earth; b) 3-D of the flight path, allowing for checking the programmed flight altitude with respect to ground level.

2-D fracture interpretation. After surface generation, the outcrop model can be exported as a 3-D textured geometry to geological modelling software or as 2-D georeferenced orthomosaic images to GIS-based software.

2.3. Fracture digitisation

Fractures in the 2-D orthomosaic images are digitised in GIS-tools such as DigiFract (Hardebol and Bertotti, 2013). Fracture lengths are manually traced, and attributes including orientation and infill can be assigned. Manual interpretation is time-intensive, but automatic tracking methods are not sufficiently sophisticated to replace manual interpretation, and require time-intensive quality-checking and manual corrections (Duelis Viana et al., 2016; Lin et al., 2015; Vasuki et al., 2014).

After digitisation, orientation, spacing and length distributions are calculated (Fig. 6). Length or height is plotted using frequency distributions (Fig. 6c,d). The orientation distribution is visualised
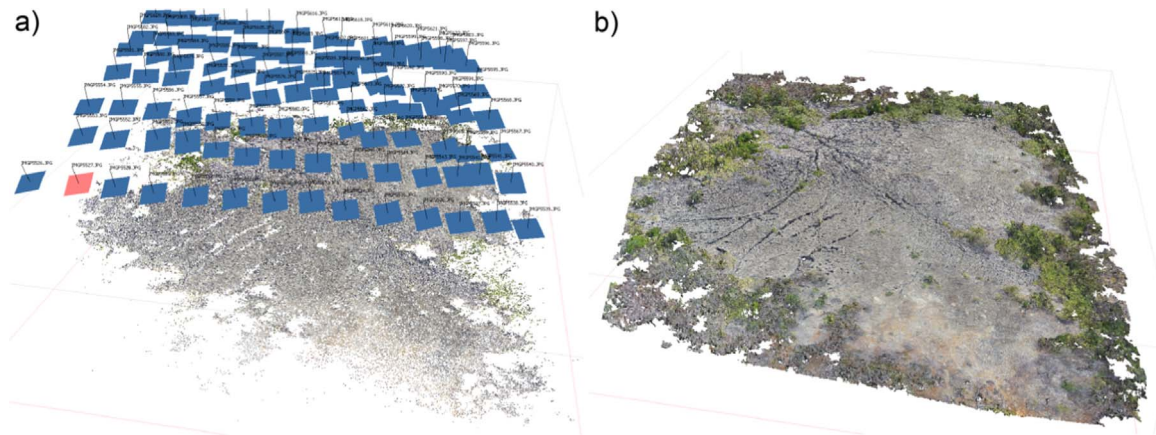
Fig. 4. Generating a 3-D outcrop model from georeferenced photographs using photogrammetry: a) Alignment of the images (rectangles) based on their GNSS position and common points extracted from the images. The image name is shown for each image (small texts); b) 3-D high-resolution point cloud of the outcrop.
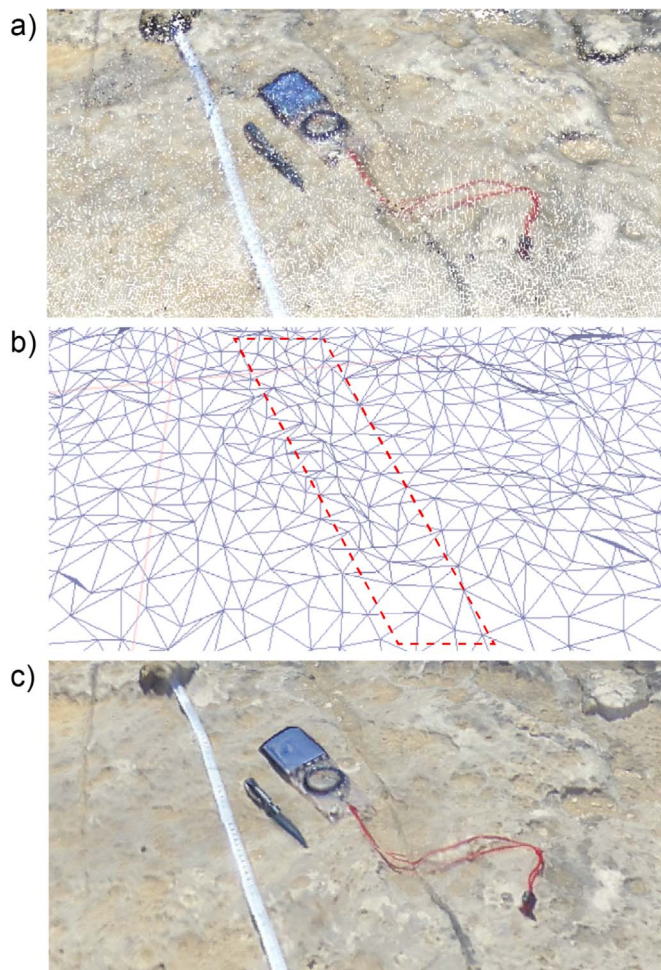

Fig. 5. Constructing a 3-D meshed surface from the point cloud: a) Detailed view of the dense point cloud with a resolution of 1.4×10^4 points per m^2, with a compass and pen for scale; b) Triangular mesh constructed for the area from (a). The mesh has a lower resolution than the point cloud, but does still indicate the main discontinuities, such as the fracture within the red dashed area; c) Texture extracted from the original photographs, projected onto the mesh.

using rose diagrams or stereoplots (Fig. 6b). Fracture spacing is calculated using a combination of methods, where P_{10} intensity, which is the 1-D fracture density measured along a line (Dershowitz, 1985), is calculated using a large amount of closely-spaced scanlines, which are projected along the entire height or length of an outcrop (Hardebol and

Bertotti, 2013). Alternatively, spacing is defined by P_{21} intensity, which is the total fracture length versus outcrop area (Dershowitz, 1985), calculated by summing the total length or height of fractures within the entire outcrop or in individual beds as a function of outcrop area (Wu and Pollard, 2002). The P_{21} method is sensitive to boundary effects, as the length of fractures that intersect the boundary cannot be fully quantified, resulting in a potential underestimation of length (Mauldon, 1998; Pahl, 1981; Zhang and Einstein, 1998). Using circular sampling windows and correction methods, this can be compensated for (Mauldon et al., 2001), but alternatively fractures that intersect the sampling boundary can be identified and excluded from the length analysis entirely.

The full spacing distribution is analysed using box-counting methods (Bonnet et al., 2001), where the outcrop is either divided into boxes with a constant area, in which P_{21} intensity is calculated (Fig. 6e), or the P_{21} intensity is calculated within a circle with a fixed centre and an increasing radius (Bonnet et al., 2001; Reith, 2015). The latter method also provides a means for characterising the Representative Elementary Area (REA), which is an indication for the optimal grid cell size for upscaled fracture flow modelling (Dershowitz and Doe, 1997; Long and Witherspoon, 1985). These methods help to identify whether the digitised networks follow power-law scaling trends (Bonnet et al., 2001; Bour and Davy, 1997; Davy et al., 1990).

The size and spacing distributions are corrected for censoring artefacts, which result from fractures that are not fully captured in the model such that their true length or height is unknown (Bonnet et al., 2001; Ortega et al., 2006). We correct for this by filtering all fractures that intersect the user-defined outcrop boundaries and by manually identifying and excluding areas obscured by for example trees. Truncation artefacts, which are related to the resolution limit of the outcrop model such that the smallest fractures are typically under-represented, cannot be corrected automatically. Truncated length and spacing scales need to be identified by the user, based on the image resolution limit.

3. Finite Element meshing and stress modelling

The 2-D fracture networks are meshed for mechanical and flow modelling, using unstructured FE meshes with explicit fractures. The meshing and the subsequent geomechanical simulations are done using ABAQUS CAE® (Dassault Systèmes®). Compared to other meshing tools, we find that this tool can handle meshing of more complex geometries, with minimal pre- and postprocessing.
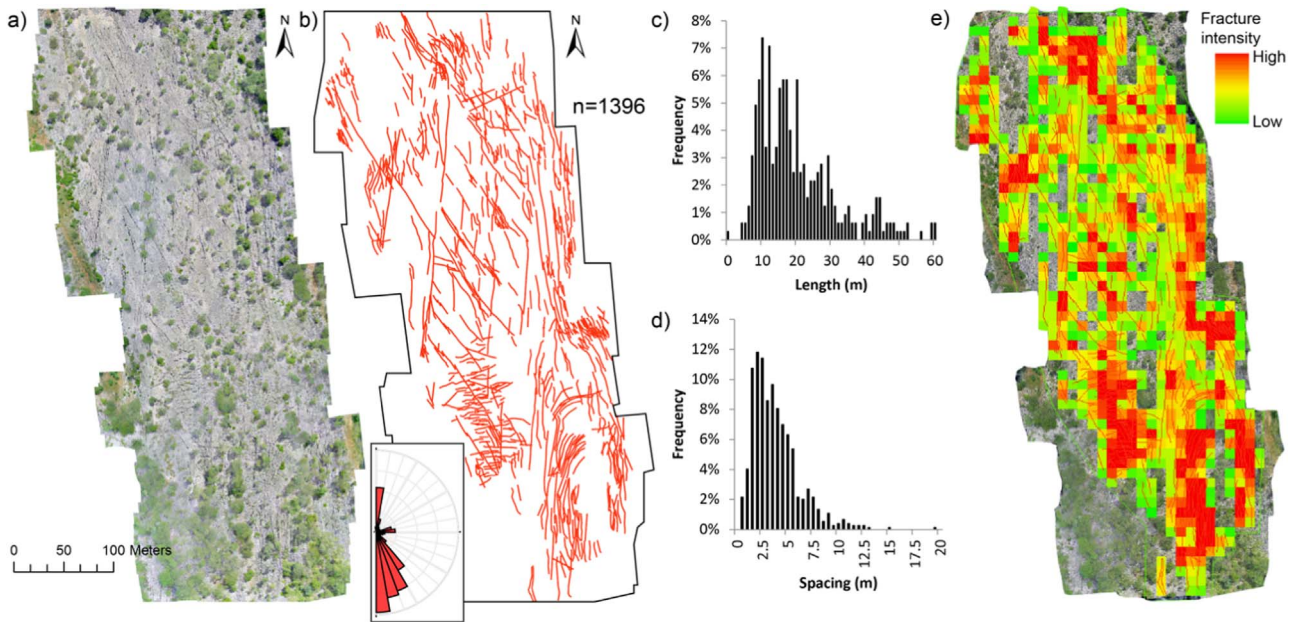
Fig. 6. Fracture digitisation and analysis in DigiFract using a 2-D orthomosaic of a carbonate pavement, constructed from 400 photographs taken from an altitude of 50 m, resulting in a orthomosaic resolution of 1.44 cm/px: a) The orthomosaic used for fracture digitisation; b) The digitised fracture network; c) Fracture length distribution; d) Fracture spacing distribution calculated using a box-counting method; e) Spatial fracture intensity calculated using box-counting.

3.1. Meshing of discrete fractures

Accurate representation of fracture connectivity and topology is essential, particularly when the matrix is close to impermeable (Fig. 7) (Hardebol et al., 2015; Sanderson and Nixon, 2015). To ensure that fracture connections and intersections are correct, most GIS tools have manual or automatic snapping options that can be used. The topology is converted to a CAD file that forms the basis for the FE model. To avoid boundary effects, rectangular model boundaries are used with an intact rock buffer zone between the fracture network and model boundary (Fig. 8). The model is meshed using quadratic plane strain elements, with refinements along the fractures (Fig. 9). To avoid singularity issues, we further refine the mesh around fracture tips. To model fracture opening and closing, fractures are represented as seams in the mesh, using a set of post-processing functions written in Python that update the mesh to generate seams (Fig. 10). A seam is generated by duplicating nodes along a seam and splitting the mesh (Fig. 11). The individual seams are generated sequentially, taking into account existing seams. Except for the intersecting seams, the output mesh is identical to the input mesh, and can be read directly into the FE simulator for analysis of the stress distribution in a complex fracture network.

3.2. Geomechanical FE model set-up

Using the ABAQUS Implicit solver, the local stress state is resolved, from which fracture apertures are derived using stress-aperture relations (Bisdom et al., 2016b). These models take into account a far-field differential stress applied to the boundaries as pressure loads (Fig. 8). Maximum and minimum principal stresses are applied perpendicular to the model boundaries in a stress initialisation step, during which movement of fracture planes and boundaries is constrained. After successful stress initialisation, the displacement conditions are released to let the model equilibrate (Fig. 8), solving for the stress tensor $\boldsymbol{\sigma}$ in fully elastic rocks (Nick et al., 2011):

$$\boldsymbol{\sigma} = \boldsymbol{D_C}(\boldsymbol{\varepsilon} - \boldsymbol{\varepsilon_0}) + \boldsymbol{\sigma_0}, \tag{1.3}$$

where $\boldsymbol{\varepsilon}$ and $\boldsymbol{\varepsilon_0}$ are the strain and initial strain vectors, $\boldsymbol{\sigma_0}$ is the initial stress vector and $\boldsymbol{D_C}$ is the material stiffness matrix:

$$\boldsymbol{D_C} = \frac{E}{(1+\nu)(1-2\nu)}\begin{bmatrix} 1-\nu & \nu & 0 \\ \nu & 1-\nu & 0 \\ 0 & 0 & 1-2\nu \end{bmatrix}, \tag{1.4}$$

with Young's modulus E and Poisson's ratio ν.

The slip tendency of fractures can be defined by a linear Mohr-Coulomb friction coefficient or non-linear behaviour, e.g. Barton-Bandis conductive shearing (Bisdom et al., 2016b), which can be
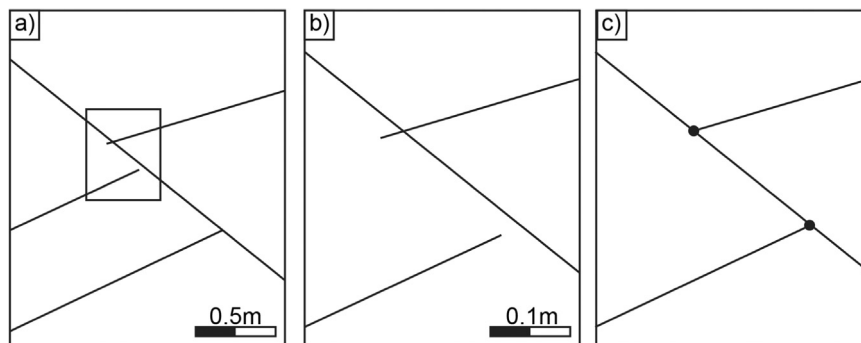

Fig. 7. Removal of minor gaps and overlaps to accurately represent the network topology: a) Three small fractures terminating against one larger fracture, with incorrect connections; b) Detail showing one overlapping segment and one segment with a gap; c) Correct fracture network interpretation using snapping.
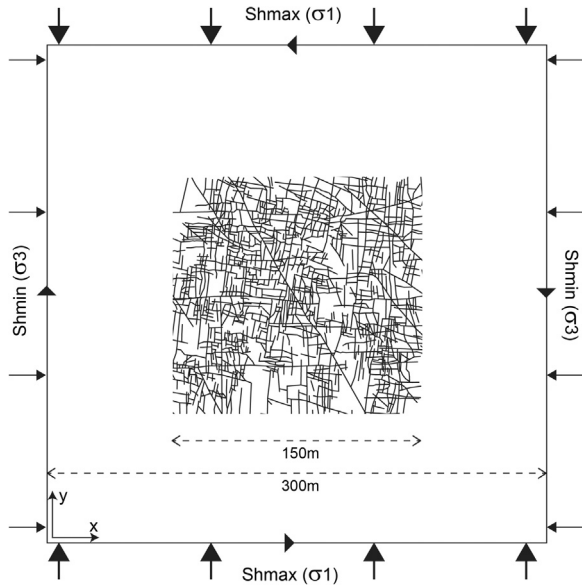
Fig. 8. Set-up of an elastic mechanical fracture network, using a 50 m×50 m fracture pattern from a carbonate outcrop in Brazil. Maximum horizontal stress σ_1 (30 MPa) is applied in the y-direction, resulting in a σ_3 of 10 MPa in the x-direction, for a Poisson's ratio of 0.3. We apply displacement boundary conditions on the centre points of each boundary to ensure symmetrical deformation.

defined by functions or look-up tables. A heterogeneous or constant pore pressure distribution can also be taken into account, as well as single-phase flow injection to account for localised changes in pore pressure over time (Bisdom et al., 2016a).

3.3. Aperture modelling

For each fracture node, stress-dependent apertures are calculated from the local normal and shear stresses in the geomechanical FE model (Fig. 12). Different stress-aperture relations can be used to calculate the corresponding spatial aperture distribution, capturing small-scale variations along individual fractures (Appendix A; Bisdom et al., 2016d). Aperture definitions that are not a function of stress, such as power-law scaling, are calculated using *Python* functions in a GIS environment, where aperture is calculated for each fracture segment based on the geometrical properties of that segment. Using the *x,y*-positions, these values are translated from the segments to the nodes of the mesh (Bisdom et al., 2016c, 2016d). Four commonly-used aperture definitions have been implemented into the workflow, but other definitions can be easily added. These four definitions are

sublinear and linear length aperture scaling predicted by LEFM, power-law scaling and Barton-Bandis conductive shearing derived from either FE models or geometrical approximations (Appendix A).

4. Flow modelling

To construct the flow model, we use the workflow from Bisdom et al. (2016b) summarised below. Here, we extend this workflow from calculating only equivalent permeability parallel to the edges of the model to calculating the full permeability tensor to derive the principal maximum and minimum permeability values.

Flow is modelled using the same FE mesh used for the geomechanical models, where the seams in the mesh have been replaced by lower-dimensional elements to which modelled fracture apertures are assigned (Bisdom et al., 2016b). In addition, the buffer zone added to avoid stress boundary effects is removed such that fractures intersect the edges of the model. We use a hybrid Finite-Element Finite-Volume (FE-FV) approach implemented in the Complex Systems Modelling Platform (CSMP++) to solve the flow equations (Matthäi et al., 2007).

Similar to Durlofsky (1991), the full equivalent permeability tensor (**k**) is computed by solving the steady state continuity equation for flow in different directions using a far-field pressure gradient applied in both horizontal directions of the rectangular 2-D pavements. Note that the superscripts 1 and 2 are used for these two problems in Eq. (1.5) and a constant viscosity (μ) is assumed. This is followed by volume-averaging (for both problems $\langle\rangle^1$, $\langle\rangle^2$) of resulted fluid velocities (u_x and u_y) and pressure gradients (∇p_x, ∇p_y) to solve for equivalent tensor permeability through:

$$\langle\nabla p\rangle\,\boldsymbol{k} = -\,\mu\langle u\rangle \Rightarrow \begin{bmatrix} \langle\nabla p_x\rangle^1 & \langle\nabla p_y\rangle^1 & 0 & 0 \\ 0 & 0 & \langle\nabla p_x\rangle^1 & \langle\nabla p_y\rangle^1 \\ \langle\nabla p_x\rangle^2 & \langle\nabla p_x\rangle^2 & 0 & 0 \\ 0 & 0 & \langle\nabla p_x\rangle^2 & \langle\nabla p_y\rangle^2 \\ 0 & 1 & -1 & 0 \end{bmatrix} \begin{Bmatrix} k_{xx} \\ k_{xy} \\ k_{yx} \\ k_{yy} \end{Bmatrix} = -\,\mu \begin{Bmatrix} \langle u_x\rangle^1 \\ \langle u_y\rangle^1 \\ \langle u_x\rangle^2 \\ \langle u_y\rangle^2 \\ 0 \end{Bmatrix}.$$

(1.5)

The maximum and minimum principal permeability values (k_{max}, k_{min}) as well as the principal direction (θ) can be calculated.

5. Application

The integrated workflow is applied to model permeability through an outcropping network of fractures in the Jandaíra Formation, which is a carbonate formation outcropping in large parts of the Potiguar Basin in NE Brazil. Large-scale fracture networks were formed predominantly during burial in a compres-

Fig. 9. Converting a deterministic fracture network into a triangular mesh: a) 150 m×142 m section extracted from an outcropping carbonate pavement in the Potiguar basin (NE Brazil); b) Meshed fracture network geometry; c) detail of the mesh showing refinement around the fracture terminations and intersections (location indicated by the white square in (b)).
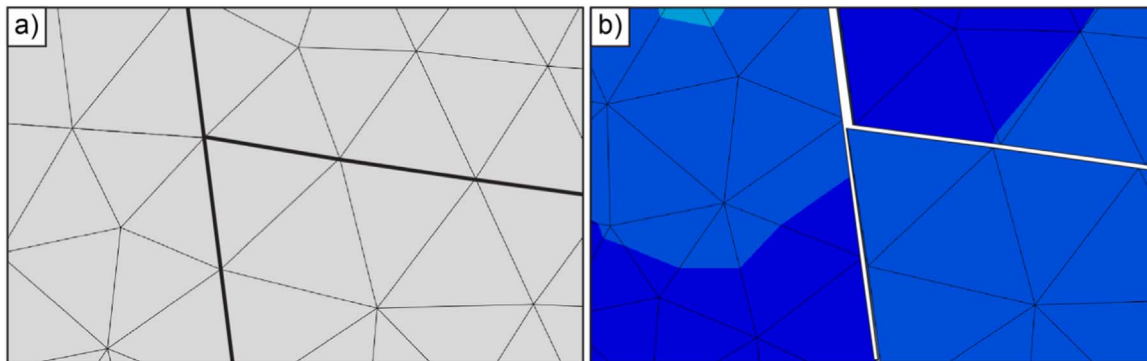
Fig. 10. Aperture in the FE models is modelled by representing the fractures as seams in the mesh, which can open or close as a function of local stress: a) Input mesh with two fractures indicated by the thick lines; b) Result after simulation, showing the stresses in the mesh and the resulting fracture opening along the seams.
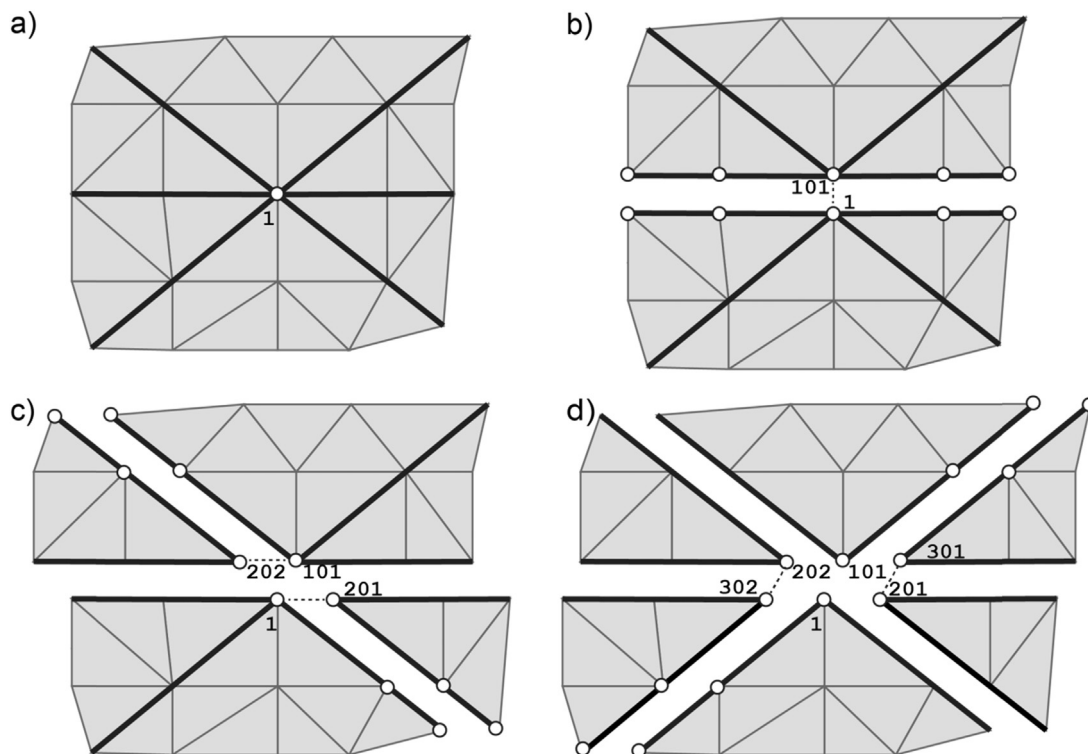

Fig. 11. Example illustrating the process of generating complex fracture intersections for three fractures that share a single intersection. The original node at this intersection, with identifier 1, is duplicated several times to generate the intersecting seams: a) Original mesh with fractures indicated by bold lines; b) Generating the first fracture by splitting nodes – node 1 is duplicated to 101; c) Second fracture requires duplication of both node 1 and 101 (1→201, 101→202); d) The third intersecting fracture requires duplication of the last two nodes formed (201→301, 202→302).

sional setting (de Graaf et al., 2017). The sub-horizontal position of the rocks provides excellent exposures of multiscale fracture patterns covering areas of several hundred by several hundred meters, which is comparable to the spacing of wells in a fractured reservoir (Bisdom et al., 2017). In conventional reservoir models, these areas are typically populated with stochastic fractures whose distributions are derived from well data or small outcrops. We use our workflow to capture and create a deterministic discrete fracture flow model, focusing on a rectangular area of a pavement in the western part of the basin in which there is a minimal impact of censoring caused by a few trees (Fig. 13). This study area is ideal for 2-D geomechanical and flow analysis, as all fractures dip perpendicular to the sub-horizontal bedding planes (Bisdom et al., 2017). Hence, spacings and lengths do not require any Terzaghi corrections, and the complete orientation distribution can be quantified by digitising fracture strikes. Geometrical analysis of fractures in the Potiguar basin is outside the scope of this work, but

presented elsewhere (Bisdom et al., 2017; de Graaf et al., 2017).

5.1. Fracture network geometry

The area of interest was imaged with the UAV at an altitude of 50 m above the ground, resulting in 90 images with a resolution of 1.44 cm/px. The model was accurately georeferenced using several GCPs, for which we measured the absolute position and the distance between the GCPs. The resulting dense point cloud covers an area of $4.1 \times 10^4 \, \mathrm{m^2}$ with a point density of $284 \, \mathrm{m^{-1}}$. The georeferenced orthomosaic has the same resolution as the individual images (1.44 cm/px; Fig. 13). Using DigiFract, we digitised 1082 fractures in a rectangular area of 150 m×142 m (Fig. 14b). Three orientation families were identified with size and spacing distributions that follow power-law scaling trends (Bisdom et al., 2017). Weathering has affected apertures and limits the view of the smallest fracture scales (i.e. smaller than 1 m), but these
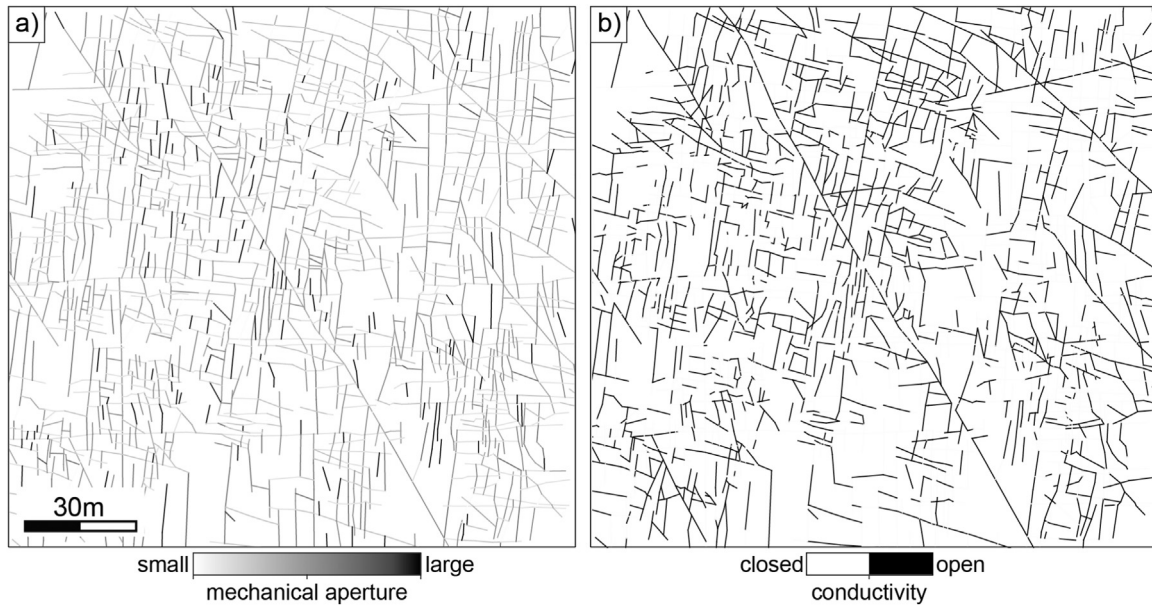
Fig. 12. Stress-induced aperture modelling: a) Mechanical aperture defined by Barton-Bandis, calculated from normal and shear stresses acting on each fracture segment, under a N-S regional σ_1 of 30 MPa and an E-W σ_3 of 10 MPa; b) Identification of hydraulically conductive fractures using the Barton-Bandis model, for the same stress boundary conditions.
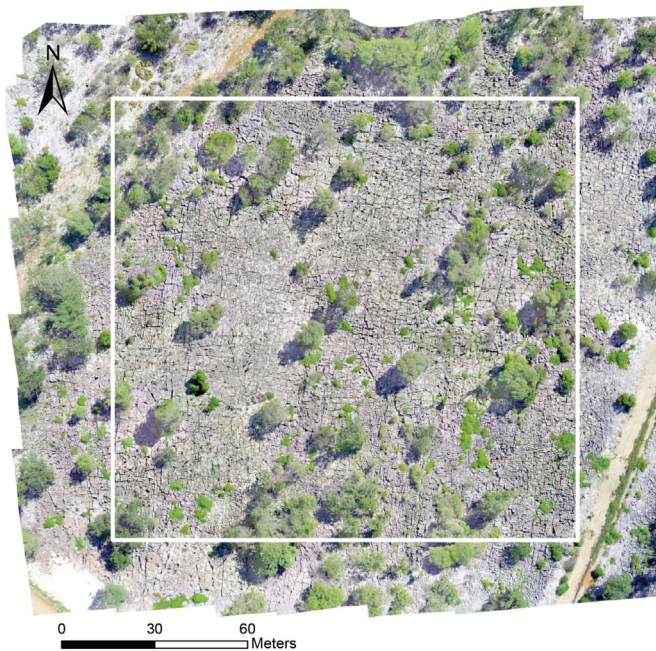

Fig. 13. High-resolution orthomosaic (1.44 cm/px resolution) of part of an outcrop in the Potiguar basin (lat/long: −5.53092°, −37.6283°) constructed from 90 georeferenced images. The white boundary indicates the domain that is considered for stress and flow modelling.

smaller length scales have only a relatively small impact on permeability compared to the large connected system of fractures. Recent weathering also created dendritic dissolution patterns, which are excluded from the analysis.

5.2. Fracture aperture distribution

Most fractures are open and free from cement, i.e. barren, but this is associated with exhumation and weathering. To define apertures representative of subsurface conditions, we use a sublinear length-aperture scaling model defined by Linear Elastic Fracture Mechanics (LEFM; Atkinson, 1984; Bisdom et al., 2016c; Lawn and Wilshaw,

1975; Olson, 2003). The far-field stress is defined by a 30 MPa σ_1 applied as pressure loads perpendicular to the north and south boundaries and a σ_3 of 10 MPa oriented E-W. These stress directions are comparable to the paleostress directions under which most of the fractures were formed (de Graaf et al., 2017). In the absence of measurements of the elastic rock properties, the rock is assumed fully elastic with a Poisson's ratio of 0.3 and a Young's modulus of 50 GPa. The model mesh consists of 5.1×10^5 triangulated elements (Fig. 14a).

The resulting aperture scales with length and stress (Fig. 14b). Aperture follows a lognormal distribution with a maximum of 2.5 mm and an average of 0.5 mm. One percent of fractures is hydraulically closed, but the majority of the network is permeable (Fig. 14c,d).

5.3. Equivalent permeability

For a 1 mD matrix, the pressure gradients in the x- and y-directions are highly heterogeneous, particularly in the x-direction (Fig. 14c,d). We quantify permeability as the ratio between equivalent and matrix permeability, which represents the contrast between matrix and fractures (Fig. 15). The ratio is high for a low matrix permeability, as flow is mainly carried by the fractures, and decreases for increasing matrix permeability. For a low permeability matrix (1 mD), fracture flow in the y-direction is more dominant than the x-direction (Fig. 15a,b), but remarkably this is reversed for higher matrix permeabilities (Fig. 15c,d).

This reversal is better quantified using the fluid velocities, which show that one large fracture percolates through the entire model in the y-direction, creating a flow pathway even when matrix permeability is low (Fig. 15a,b). There are several large E-W striking fractures with large apertures, but they do not fully percolate the model, limiting their impact in a low-permeability matrix.

This change in permeability is better explained by calculating the full permeability tensor (Fig. 16). For matrix permeabilities below 100 mD, maximum permeability is in a NE-SW direction. In this domain, permeability is controlled by fracture flow. For increasing matrix permeability, flow is carried by a mix of fractures and matrix, and the maximum permeability rotates to ENE-WSW, remaining anisotropic. Only when matrix permeability is larger than several Darcy, flow is fully carried by the matrix and permeability becomes isotropic. However, for most models, the highly-connected high-intensity fracture network controls flow either completely or partly.
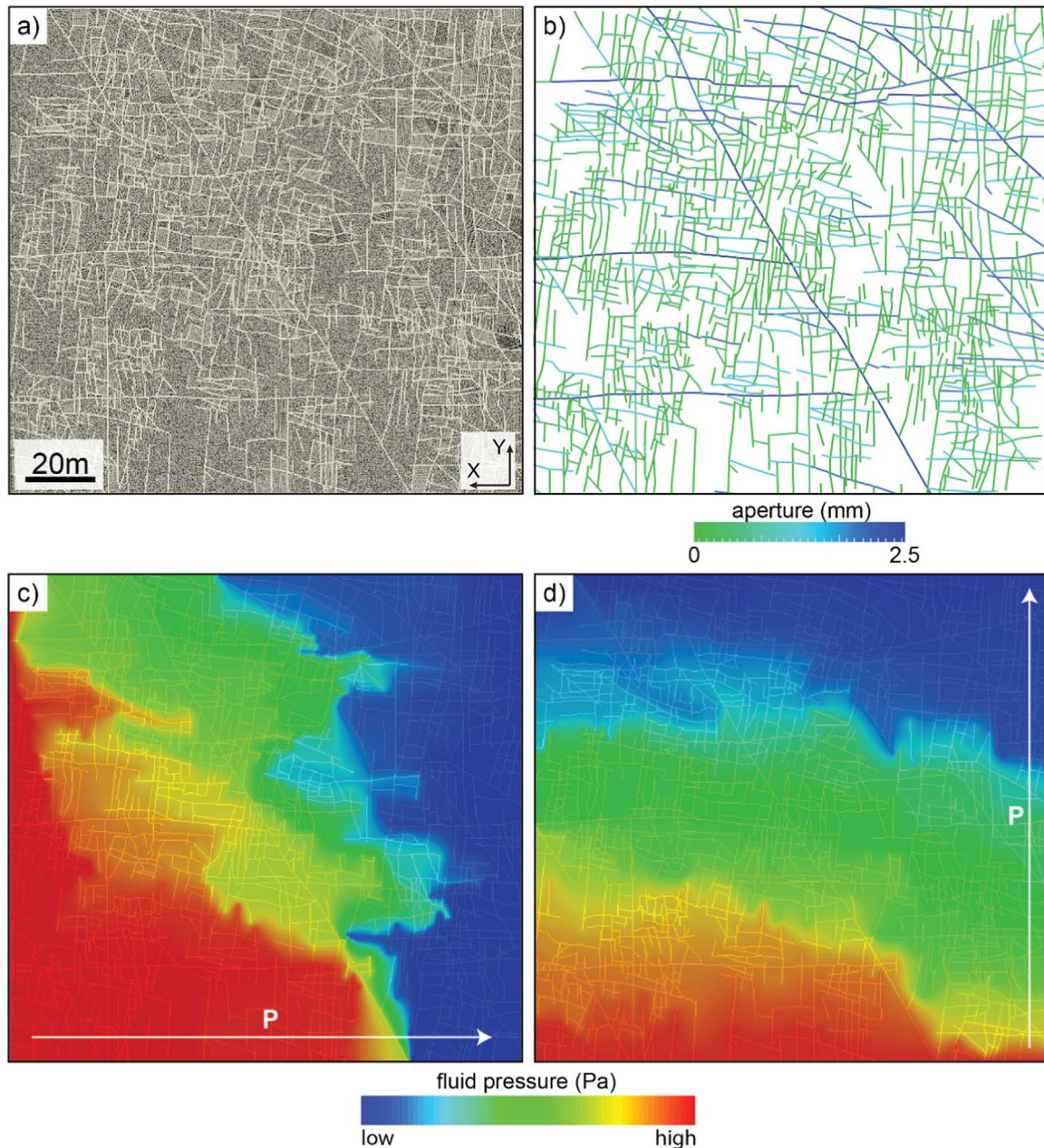
Fig. 14. Aperture and permeability results: a) 2-D mesh with $5.1×10^5$ triangular matrix elements and $3.3×10^4$ linear fracture elements; b) Aperture distribution derived from the local stress state assuming sublinear length-aperture scaling relations with a maximum horizontal stress oriented in the y-direction; c) Fluid pressure gradient in the x-direction (indicated by arrow) for a 1 mD matrix permeability; d) Fluid pressure in the y-direction.

6. Discussion

6.1. From outcrops to representative subsurface flow models

Contrary to other studies, the presented workflow uses only the outcropping network geometry as input for deterministic flow models, not taking into account outcropping apertures. Instead, we use geomechanical FE models to solve the stress state around the fracture network, based on estimates of subsurface stress conditions and rock properties. These geomechanical parameters can typically be derived from subsurface datasets, albeit with uncertainty ranges. However, the applied methodology is fast, allowing for the inclusion of uncertainty ranges. The resulting stress states are used to calculate aperture, using different stress-aperture relations (Bisdom et al., 2016d). This combi-nation of outcropping geometries and subsurface stress states and aperture distributions results in models that are more representative of fractured reservoir permeability compared to analogue studies that use apertures of exhumed barren fractures or assume a constant aperture for the entire network (Makedonska et al., 2016).

In terms of data acquisition, laser scanning of outcrops is an alternative method that provides deterministic representations of entire outcrops, but photogrammetry offers more flexibility (Hodgetts, 2013). Through the use of deterministic 2-D patterns rather than stochastic fracture networks derived from 1-D distributions, more realistic estimates of permeability can be made. Stochastic models typically contain mutually crosscutting networks of fractures resulting in highly connected networks with high permeabilities, which does not correspond to observations of permeability heterogeneity typically observed in fractured reservoirs. The studied deterministic pattern better represents natural fracture topology with terminating rather than fully crosscutting fractures (Hardebol et al., 2015; Sanderson and Nixon, 2015).
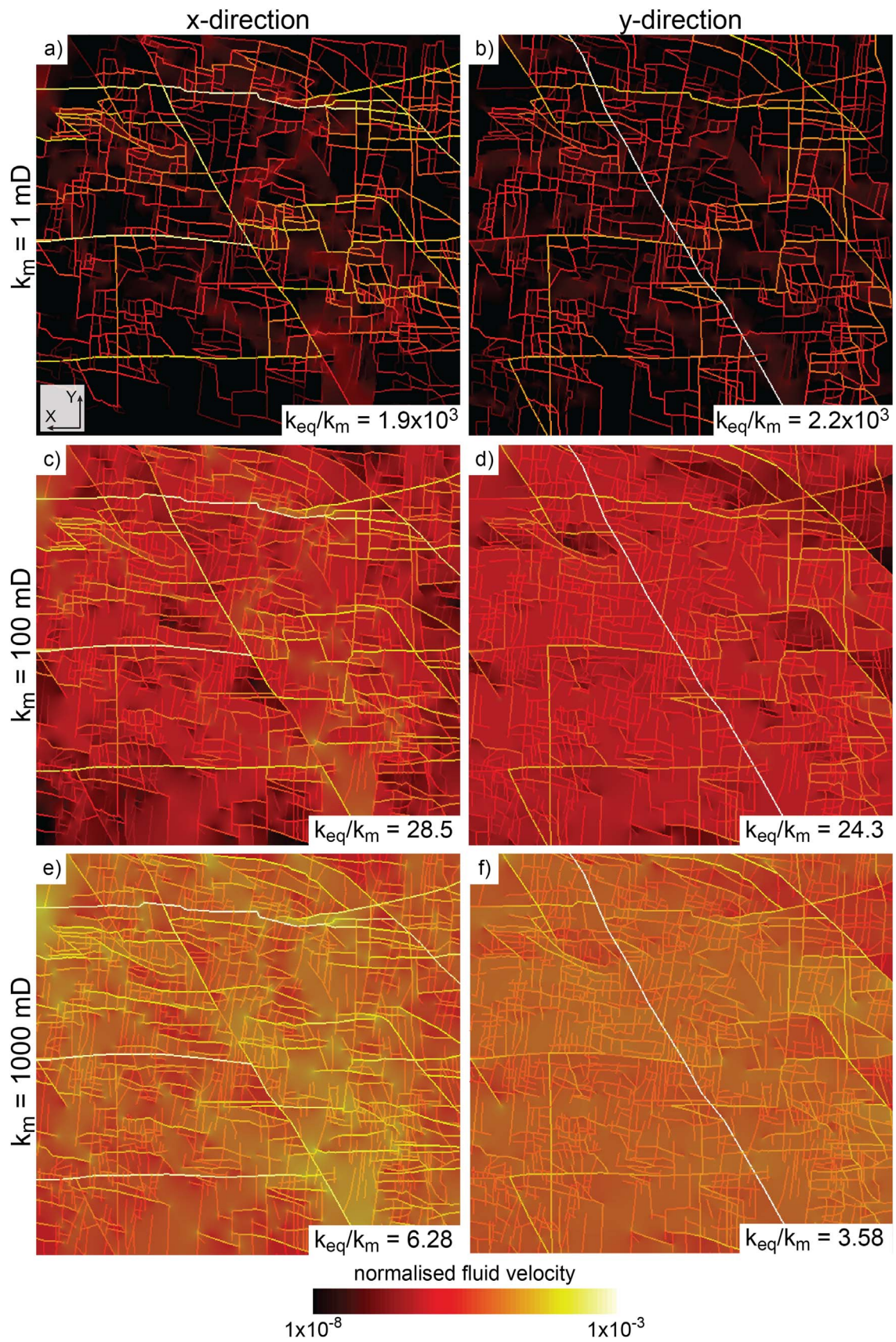
Fig. 15. Fluid velocity magnitudes under far-field pressure gradient in the x-direction (a, c, e) and y-direction (b, d, f) for different matrix permeabilities.
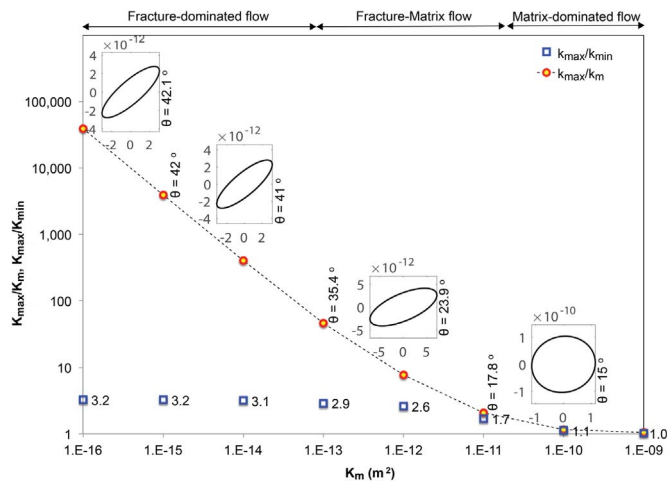
Fig. 16. Maximum permeability versus matrix permeability for a range of matrix permeabilities. The direction of maximum permeability is indicated by the ellipses and θ, measured from the East. The ratio between minimum and maximum permeability remains relatively constant except for Darcy-scale flow, where permeability is completely controlled by matrix flow.

6.2. Lessons for reservoir-scale flow modelling

The studied fracture network from the Potiguar basin contains predominantly N-S and E-W striking fractures that form an orthogonal pattern. Orthogonal patterns are observed in many fractured outcrops and are assumed to be present in many subsurface reservoirs (Bai et al., 2002). In reservoir-scale flow models, these patterns are upscaled to effective properties in the two dominant fracture directions that are assumed to be representative of fracture permeability, comparable to the equivalent permeability in the x- and y-directions. However, by only considering flow in two directions, permeability is underestimated in this example, as for a 1 mD matrix permeability, the permeability ratio in x- and y-directions is 1.9×10^3 and 2.2×10^3 respectively, whereas the maximum ratio is 3.9×10^3 in the NE-SW direction. Even for these relatively homogeneous orthogonal networks, the absolute maximum permeability cannot be accurately determined using conventional upscaling. The outcrop-derived 2-D permeability tensor models can be used to determine the principal permeabilities of discrete fracture networks covering several grid cells, as a more accurate alternative to quantify permeability compared to ODA upscaling (Oda, 1985). These flow models also help to identify different fracture-matrix permeability domains, which can be used to better characterise fractured reservoir flow domains. To further bridge the gap between discrete fracture models and reservoir-scale continuum models, hybrid upscaling techniques can be used (Egya et al., 2016; Shah et al., 2016).

7. Conclusions

Outcrops provide a wealth of data for studying and modelling of

fracture networks, which cannot be fully captured with 1-D scanlines, as these only capture spacing and aperture of one orientation set. LiDAR on the other hand captures entire outcrops at a high resolution, but this method has limited flexibility in terms of the type of outcrops it can be applied to and in terms of processing (Hodgetts, 2013). The presented workflow enables fast generation of highly detailed realistic fracture networks for use of geomechanical and flow modelling, variations of which have been applied to study different aspects of fracture and fracture-matrix flow (e.g. Aljuboori et al., 2015; Arnold et al., 2016; Bisdom et al., 2016c; Egya et al., 2016; Muhammad, 2016; Shah et al., 2016).

We use fracture patterns derived from these models for geomechanical and flow modelling of discrete fractures on a scale that is representative of part of a fractured reservoir, spanning an area of several conventional reservoir grid cells. The geomechanical model solves the local stress state within the fracture network, which is used to model aperture using a range of stress-aperture relations. The flow models consider matrix and fracture flow. Although the fluid pressure in the directions parallel to the model boundaries can be used to quantify relative permeability differences between different models, it is not representative of the true principal permeabilities, even in an orthogonal network where fractures strike mainly parallel to the x- and y-directions. The presented workflow allows for fast quantification of the full permeability tensor in domains covering several conventional simulator grid cells using realistic fracture patterns digitised from outcrops, with minimal pre-processing and no upscaling.

Appendix A. – Summary of aperture methods

(Sub-)linear length-aperture scaling

Linear Elastic Fracture Mechanics (LEFM) predicts that aperture scales (sub)linearly with length during propagation of fractures (Atkinson, 1984; Olson, 2003; Pollard and Segall, 1987). Maximum opening at the centre of the fracture, d_{max}, is defined by fracture toughness K_C, the Poisson's ratio ν, Young's modulus E and fracture length L:

$$d_{max} = \frac{K_C(1-\nu^2)}{E\sqrt{\pi/8}}\sqrt{L},$$

where K_C is a function of driving stress $\Delta\sigma_I$ and fracture length:

$K_C = \Delta\sigma_I\sqrt{\pi L/2}$.

Discussion remains on whether aperture scales linear or sublinear with length, which has large implications for apertures of relatively large fractures (Olson, 2003; Olson and Schultz, 2011; Scholz, 2011; Vermilye and Scholz, 1995). The impact of linear versus sublinear scaling on permeability is investigated in Bisdom et al. (2016d).

Power-law scaling

Outcrop studies typically find that fracture lengths follow power-law scaling distributions (e.g. Bonnet et al., 2001; Bour and Davy, 1997). This, combined with the linear length-aperture scaling model, implies that aperture also follows power-law scaling relations. Power-law scaling of apertures is commonly observed in outcrops (Hooker et al., 2014, 2009; Ortega et al., 2006), although the relation with length is rarely studied in outcrops. Instead, the aperture distributions are defined independent of other geometrical or geomechanical parameters, through a power-law function:

$F = aX^{-b}$,

where F is the cumulative frequency, a is a density constant and b is the power-law scaling exponent (Bonnet et al., 2001). Power-law aperture distributions are the preferred method of defining aperture in industry fractured reservoir models, but they are rarely related to any other geometrical parameter. As a result, short fractures may be assigned unrealistically large apertures (Bisdom et al., 2016d).

Barton-Bandis

Whereas (sub-)linear length-aperture scaling predicts opening during propagation over geological times, Barton-Bandis describes present-day opening in the current stress field, assuming that fractures have irregular walls that result in conductive fractures when shearing occurs, even when fluid pressures are low (Bandis, 1980; Bandis et al., 1983; Barton, 1982; Barton and Bandis, 1980; Barton and Choubey, 1977). Mechanical aperture E_n is a function of an intrinsic initial aperture E_O, maximum closure v_m, toughness K_{ni} and driving stress $\Delta\sigma_I$ (e.g. Barton, 2014).

$$E_n = E_0 - \left(\frac{1}{v_m} + \frac{K_{ni}}{\Delta\sigma_I}\right)^{-1}.$$

Hydraulic aperture e is a function of mechanical aperture, the Joint Roughness Coefficient (JRC) and the ratio between shear (u_{geom}) and peak shear (u_{peak}) displacement (Olsson and Barton, 2001).

$$e = \begin{cases} \frac{E_n^2}{JRC^{2.5}} \text{ for } \frac{u_{geom}}{u_{peak}} \leq 0.75 \\ \sqrt{E_n}\, JRC_{mob} \text{ for } \frac{u_{geom}}{u_{peak}} \geq 1 \end{cases}.$$

This aperture model is strongly dependent on the local normal and shear stress acting on each fracture segment, which is most accurately determined using geomechanical Finite-Element models with discrete fractures (Bisdom et al., 2016b; Lei et al., 2014).

Alternatively, an approximation of Barton-Bandis apertures can be made without use of numerical models. Using a far field stress and fracture geometry, aperture can be approximated (Bisdom et al., 2016c). This model is strongly dependent on stress angle α between fracture strike and σ_1:

$\sigma_{n,angle} = 0.0054\sigma_I\alpha + 1.5186\sigma_I^{0.723}$.

Normal stress is further corrected for length L and spacing S:

$\sigma_{n,geom} = 0.996S^{-0.008}\sigma_{n,angle}(-0.083\ln L + 1.055)$.

Shear displacement is also defined as a function of length and stress angle:

$u_{geom} = L\sigma_I\alpha(-9.07\cdot10^{-8}\alpha + 8.1\cdot10^{-6})$.

Appendix B. Supporting information

Supplementary data associated with this article can be found in the online version at doi:10.1016/j.cageo.2017.02.019. These data include Google maps of the most important areas described in this article.

References

Aljuboori, F., Corbett, P., Bisdom, K., Bertotti, G., Geiger, S., 2015. Using outcrop data for geological well test modelling in fractured reservoirs. In: Proceedings of the 77th EAGE Conference and Exhibition 2015. doi:10.3997/2214-4609.201413037.

Arnold, D., Demyanov, V., Christie, M., Bakay, A., Gopa, K., 2016. Optimisation of decision making under uncertainty throughout field lifetime: a fractured reservoir example. Comput. Geosci. 95, 123–139. http://dx.doi.org/10.1016/j.cageo.2016.07.011.

Atkinson, B.K., 1984. Subcritical crack growth in geological materials. J. Geophys. Res. 89, 4077. http://dx.doi.org/10.1029/JB089iB06p04077.

Baghbanan, A., Jing, L., 2008. Stress effects on permeability in a fractured rock mass with correlated fracture length and aperture. Int. J. Rock Mech. Min. Sci. 45, 1320–1334. http://dx.doi.org/10.1016/j.ijrmms.2008.01.015.

Bai, T., Maerten, L., Gross, M.R., Aydin, A., 2002. Orthogonal cross joints: do they imply a regional stress rotation? J. Struct. Geol. 24, 77–88. http://dx.doi.org/10.1016/S0191-8141(01)00050-5.

Bandis, S., 1980. Experimental Studies of Scale Effects on Shear Strength and Deformation of Rock Joints. University of Leeds. http://dx.doi.org/10.12681/eadd/4686.

Bandis, S.C., Lumsden, A.C., Barton, N.R., 1983. Fundamentals of rock joint deformation. Int. J. Rock Mech. Min. Sci. Geomech. Abstr. 20, 249–268. http://dx.doi.org/10.1016/0148-9062(83)90595-8.

Barton, N., 2014. Non-linear behaviour for naturally fractured carbonates and frac-stimulated gas-shales. First Break 32, 51–66. http://dx.doi.org/10.3997/1365-2397.2014011.

Barton, N., 1982. Modelling rock joint behaviour from in situ block tests: Implications for

nuclear waste repository design. Columbus, OH.

Barton, N., Bandis, S., 1980. Some effects of scale on the shear strength of joints. Int. J. Rock Mech. Mining Sci. Geomech. Abstr., 69–73. http://dx.doi.org/10.1016/0148-9062(80)90009-1.

Barton, N., Bandis, S., Bakhtar, K., 1985. Strength, deformation and conductivity coupling of rock joints. Int. J. Rock Mech. Min. Sci. Geomech. Abstr. 22, 121–140. http://dx.doi.org/10.1016/0148-9062(85)93227-9.

Barton, N., Choubey, V., 1977. The shear strength of rock joints in theory and practice. Rock Mech. Felsmech. Mec. Des. Roches 10, 1–54. http://dx.doi.org/10.1007/BF01261801.

Belayneh, M.W., Matthäi, S.K., Blunt, M.J., Rogers, S.F., 2009. Comparison of deterministic with stochastic fracture models in water-flooding numerical simulations. Am. Assoc. Pet. Geol. Bull. 93, 1633–1648. http://dx.doi.org/10.1306/07220909031.

Bemis, S.P., Micklethwaite, S., Turner, D., James, M.R., Akciz, S., Thiele, S.T., Bangash, H.A., 2014. Ground-based and UAV-based photogrammetry: a multi-scale, high-resolution mapping tool for structural geology and paleoseismology. J. Struct. Geol. 69, 163–178. http://dx.doi.org/10.1016/j.jsg.2014.10.007.

Bisdom, K., Baud, E., Estrada, S., Sanz-Perl, Y., Gauthier, B., Bertotti, G., 2016a. Coupled stress-fluid pressure modelling of stimulated rock volume in shale – impact of natural fractures and beef, In: Proceedings of the 78th EAGE Conference & Exhibition. EAGE, Vienna, Austria.

Bisdom, K., Bertotti, G., Bezerra, F.H., 2017. Inter-well scale natural fracture geometry and permeability variations in low-deformation carbonate rocks. J. Struct. Geol. 97, 23–36. http://dx.doi.org/10.1016/j.jsg.2017.02.011.

Bisdom, K., Bertotti, G., Nick, H.M., 2016b. The impact of in-situ stress and outcrop-based fracture geometry on hydraulic aperture and upscaled permeability in fractured reservoirs. Tectonophysics 690, 63–75. http://dx.doi.org/10.1016/j.tecto.2016.04.006.

Bisdom, K., Bertotti, G., Nick, H.M., 2016c. A geometrically based method for predicting stress-induced fracture aperture and flow in discrete fracture networks. Am. Assoc. Pet. Geol. Bull. 100, 1075–1097. http://dx.doi.org/10.1306/02111615127.

Bisdom, K., Bertotti, G., Nick, H.M., 2016d. The impact of different aperture distribution models and critical stress criteria on equivalent permeability in fractured rocks. J. Geophys. Res. Solid Earth 121, 4045–4063. http://dx.doi.org/10.1002/2015JB011657.

Bisdom, K., Gauthier, B.D.M., Bertotti, G., Hardebol, N.J., 2014. Calibrating discrete fracture-network models with a carbonate three-dimensional outcrop fracture network: implications for naturally fractured reservoir modeling. Am. Assoc. Pet. Geol. Bull. 98, 1351–1376. http://dx.doi.org/10.1306/02031413060.

Bond, C.E., Shackleton, J.R., Wild, T., 2015. From Field Fractures to Reservoir Prediction: Utilizing Drones, Virtual Outcrop and Digital Data Analysis to Input Into Discrete Fracture Network (DFN) Models, In: Proceedings of AAPG Annual Convention and Exhibition. Denver, Colorado.

Bonnet, E., Bour, O., Odling, N.E., Davy, P., Main, I., Cowie, P., Berkowitz, B., 2001. Scaling of fracture systems in geological media. Rev. Geophys. 39, 347–383. http://dx.doi.org/10.1029/1999RG000074.

Bour, O., Davy, P., 1997. Connectivity of random fault networks following a power law fault length distribution. Water Resour. Res. 33, 1567–1583. http://dx.doi.org/10.1029/96WR00433.

Cottereau, N., Garcia, M.H., Gosselin, O.R., Vigier, L., 2010. Effective fracture network permeability: comparative study of calculation methods, In: Proceedings of SPE EUROPEC/EAGE Annual Conference and Exhibition. Society of Petroleum Engineers, Barcelona, Spain. doi:10.2118/131126-ms.

Davy, P., Sornette, A., Sornette, D., 1990. Some consequences of a proposed fractal nature of continental faulting. Nature 348, 56–58. http://dx.doi.org/10.1038/348056a0.

de Graaf, S., Reijmer, J.J.G., Bertotti, G.V., Bezerra, F.H.R., Cazarin, C.L., Bisdom, K., Vonhof, H.B., 2017. Fracturing and calcite cementation controlling fluid flow in the shallow-water carbonates of the Jandaíra Formation. Brazil. Mar. Pet. Geol. 80, 382–393. http://dx.doi.org/10.1016/j.marpetgeo.2016.12.014.

Dershowitz, W., 1985. Rock Joint Systems (Ph.D. Thesis). MIT, Massachusetts Institute of Technology, Cambridge, MA., USA.

Dershowitz, W., Doe, T., 1997. Analysis of heterogeneously connected rock masses by forward modeling of fractional dimension flow behavior. Int. J. Rock Mech. Min. Sci. 34, 61.e1–61.e19. http://dx.doi.org/10.1016/S1365-1609(97)00237-2.

Duelis Viana, C., Endlein, A., Ademar da Cruz Campanha, G., Henrique Grohmann, C., 2016. Algorithms for extraction of structural attitudes from 3D outcrop models. Comput. Geosci. 90, 112–122. http://dx.doi.org/10.1016/j.cageo.2016.02.017.

Durlofsky, L.J., 1991. Numerical calculation of equivalent grid block permeability tensors for heterogeneous porous media. Water Resour. Res. 27, 699–708. http://dx.doi.org/10.1029/91WR00107.

Egya, D., Geiger, S., Corbett, P., Bisdom, K., Bertotti, G., Bezerra, H., 2016. Assessing the Validity and Limitations of Dual- porosity Models Using Geological Well Testing for Fractured Formations, In: Proceedings of the 78th EAGE Conference & Exhibition. EAGE, Vienna, Austria.

Fabuel-Perez, I., Hodgetts, D., Redfern, J., 2010. Integration of digital outcrop models (DOMs) and high resolution sedimentology – workflow and implications for geological modelling: Oukaimeden Sandstone Formation, High Atlas (Morocco). Pet. Geosci. 16, 133–154. http://dx.doi.org/10.1144/1354-079309-820.

Geiger, S., Hehmeyer, O., Agada, S., Mutti, M., Benson, G., Shekhar, R., Toigulova, G., Chen, F., Christ, N., Amour, F., Agar, S., Immenhauser, A., 2013. Deciphering the fundamental controls of flow in carbonates using numerical well-testing, production optimisation, and 3D high-resolution outcrop analogues for fractured carbonate reservoirs. In: Proceedings of 75th EAGE Conference & Exhibition Incorporating SPE EUROPEC 2013. Society of Petroleum Engineers. doi:10.2118/164805-MS.

Geiger, S., Matthäi, S., 2012. What can we learn from high-resolution numerical simulations of single- and multi-phase fluid flow in fractured outcrop analogues? Geol. Soc. Lond., Spec. Publ. 374, 125–144. http://dx.doi.org/10.1144/SP374.8.

Hardebol, N.J., Bertotti, G., 2013. DigiFract: a software and data model implementation for flexible acquisition and processing of fracture data from outcrops. Comput. Geosci. 54, 326–336. http://dx.doi.org/10.1016/j.cageo.2012.10.021.

Hardebol, N.J., Maier, C., Nick, H., Geiger, S., Bertotti, G., Boro, H., 2015. Multiscale fracture network characterization and impact on flow: a case study on the Latemar carbonate platform. J. Geophys. Res. Solid Earth 120, 8197–8222. http://dx.doi.org/10.1002/2015JB011879.

Harwin, S., Lucieer, A., 2012. Assessing the accuracy of georeferenced point clouds produced via multi-view stereopsis from Unmanned Aerial Vehicle (UAV) imagery. Remote Sens. 4, 1573–1599. http://dx.doi.org/10.3390/rs4061573.

Hodgetts, D., 2013. Laser scanning and digital outcrop geology in the petroleum industry: a review. Mar. Pet. Geol. 46, 335–354. http://dx.doi.org/10.1016/j.marpetgeo.2013.02.014.

Hooker, J.N., Gale, J.F.W., Gomez, L.A., Laubach, S.E., Marrett, R., Reed, R.M., 2009. Aperture-size scaling variations in a low-strain opening-mode fracture set, Cozzette Sandstone, Colorado. J. Struct. Geol. 31, 707–718. http://dx.doi.org/10.1016/j.jsg.2009.04.001.

Hooker, J.N., Laubach, S.E., Marrett, R., 2014. A universal power-law scaling exponent for fracture apertures in sandstones. Geol. Soc. Am. Bull. 126, 1340–1362. http://dx.doi.org/10.1130/B30945.1.

James, M.R., Robson, S., 2012. Straightforward reconstruction of 3D surfaces and topography with a camera: accuracy and geoscience application. J. Geophys. Res. Earth Surf. 117, 1–17. http://dx.doi.org/10.1029/2011JF002289.

Jonoud, S., Jackson, M.D., 2008. Validity of steady-state upscaling techniques. SPE Reserv. Eval. Eng. 11, 405–416. http://dx.doi.org/10.2118/100293-PA.

Karimi-Fard, M., Durlofsky, L.J., 2016. A general gridding, discretization, and coarsening methodology for modeling flow in porous formations with discrete geological features. Adv. Water Resour., 354–372. http://dx.doi.org/10.1016/j.advwatres.2016.07.019.

Lang, P.S., Paluszny, A., Zimmerman, R.W., 2014. Permeability tensor of three-dimensional fractured porous rock and a comparison to trace map predictions. J. Geophys. Res. Solid Earth 119, 6288–6307. http://dx.doi.org/10.1002/2014JB011027.

Lawn, B.R., Wilshaw, T.R., 1975. Fracture of Brittle Solids. Cambridge University Press.

Lei, Q., Latham, J., Xiang, J., Tsang, C.-F., 2015. Polyaxial stress-induced variable aperture model for persistent 3D fracture networks. Geomech. Energy Environ. 1, 34–47. http://dx.doi.org/10.1016/j.gete.2015.03.003.

Lei, Q., Latham, J.-P., Xiang, J., Tsang, C.-F., Lang, P., Guo, L., 2014. Effects of geomechanical changes on the validity of a discrete fracture network representation of a realistic two-dimensional fractured rock. Int. J. Rock Mech. Min. Sci. 70, 507–523. http://dx.doi.org/10.1016/j.ijrmms.2014.06.001.

Lei, Q., Wang, X., Xiang, J., Latham, J.-P., 2016. Influence of stress on the permeability of a three-dimensional fractured sedimentary layer. 50th US Rock Mech./Geomech. Symp. 586.

Lin, Y., Jiang, M., Yao, Y., Zhang, L., Lin, J., 2015. Use of UAV oblique imaging for detection of individual trees in residential environments. Urban For. Urban Green. 14, 404–412. http://dx.doi.org/10.1016/j.ufug.2015.03.003.

Long, J.C.S., Witherspoon, P.A., 1985. The relationship of the degree of interconnection to permeability in fracture networks. J. Geophys. Res. 90, 3087. http://dx.doi.org/10.1029/JB090iB04p03087.

Mahmud, K., Mariethoz, G., Treble, P.C., Baker, A., 2015. Terrestrial LiDAR survey and morphological analysis to identify infiltration properties in the Tamala Limestone, Western Australia. IEEE J. Sel. Top. Appl. Earth Obs. Remote Sens. 8, 4871–4881. http://dx.doi.org/10.1109/JSTARS.2015.2451088.

Makedonska, N., Hyman, J.D., Karra, S., Painter, S.L., Gable, C.W., Viswanathan, H.S., 2016. Evaluating the effect of internal aperture variability on transport in kilometer scale discrete fracture networks. Adv. Water Resour. 94, 486–497. http://dx.doi.org/10.1016/j.advwatres.2016.06.010.

Martinez-Landa, L., Carrera, J., Pérez-Estaún, A., Gomez, P., Bajos, C., 2016. Structural geology and geophysics as a support to build a hydrogeologic model of granite rock. Solid Earth 7, 881–895. http://dx.doi.org/10.5194/se-7-881-2016.

Matthäi, S.K., Belayneh, M., 2004. Fluid flow partitioning between fractures and a permeable rock matrix. Geophys. Res. Lett., 31. http://dx.doi.org/10.1029/2003GL019027.

Matthäi, S.K., Geiger, S., Roberts, S.G., Paluszny, A., Belayneh, M., Burri, A., Mezentsev, A., Lu, H., Coumou, D., Driesner, T., Heinrich, C.A., 2007. Numerical simulation of multi-phase fluid flow in structurally complex reservoirs. Geol. Soc. Lond., Spec. Publ. 292, 405–429. http://dx.doi.org/10.1144/SP292.22.

Mauldon, M., 1998. Estimating mean fracture trace length and density from observations in convex windows. Rock. Mech. Rock Eng. 31, 201–216. http://dx.doi.org/10.1007/s006030050021.

Mauldon, M., Dunne, W.M., Rohrbaugh, M.B., 2001. Circular scanlines and circular windows: new tools for characterizing the geometry of fracture traces. J. Struct. Geol. 23, 247–258. http://dx.doi.org/10.1016/S0191-8141(00)00094-8.

Muhammad, F., 2016. Geological Well Testing in Fractured Carbonate Reservoir. Heriot Watt University, Edinburgh, UK.

Nejati, M., Paluszny, A., Zimmerman, R.W., 2016. A finite element framework for modeling internal frictional contact in three-dimensional fractured media using unstructured tetrahedral meshes. Comput. Methods Appl. Mech. Eng. 306, 123–150. http://dx.doi.org/10.1016/j.cma.2016.03.028.

Nelson, R.A., 2001. Geologic Analysis of Naturally Fractured Reservoirs. Gulf Professional Publishing, Woburn, MA, USA, 101–124.

Nick, H.M., Matthäi, S.K., 2011a. A hybrid finite-element finite-volume method with

embedded discontinuities for solute transport in heterogeneous media. Vadose Zo. J. 10, 299. http://dx.doi.org/10.2136/vzj2010.0015.

Nick, H.M., Matthäi, S.K., 2011b. Comparison of three FE-FV numerical schemes for single- and two-phase flow simulation of fractured porous media. Transp. Porous Media 90, 421–444. http://dx.doi.org/10.1007/s11242-011-9793-y.

Nick, H.M., Paluszny, A., Blunt, M.J., Matthai, S.K., 2011. Role of geomechanically grown fractures on dispersive transport in heterogeneous geological formations. Phys. Rev. E 84, 56301. http://dx.doi.org/10.1103/PhysRevE.84.056301.

Oda, M., 1985. Permeability tensor for discontinuous rock masses. Géotechnique 35, 483–495.

Olson, J.E., 2003. Sublinear scaling of fracture aperture versus length: an exception or the rule? J. Geophys. Res. Solid Earth 108, 2413. http://dx.doi.org/10.1029/2001JB000419.

Olson, J.E., Laubach, S.E., Lander, R.H., 2009. Natural fracture characterization in tight gas sandstones: integrating mechanics and diagenesis. Am. Assoc. Pet. Geol. Bull. 93, 1535–1549. http://dx.doi.org/10.1306/08110909100.

Olson, J.E., Schultz, R.A., 2011. Comment on "A note on the scaling relations for opening mode fractures in rock" by C.H. Scholz. J. Struct. Geol. 33, 1523–1524. http://dx.doi.org/10.1016/j.jsg.2011.07.004.

Olsson, R., Barton, N., 2001. An improved model for hydromechanical coupling during shearing of rock joints. Int. J. Rock Mech. Min. Sci. 38, 317–329. http://dx.doi.org/10.1016/S1365-1609(00)00079-4.

Ortega, O.J., Marrett, R.A., Laubach, S.E., 2006. A scale-independent approach to fracture intensity and average spacing measurement. Am. Assoc. Pet. Geol. Bull. 90, 193–208. http://dx.doi.org/10.1306/08250505059.

Pahl, P.J., 1981. Estimating the mean length of discontinuity traces. Int. J. Rock Mech. Min. Sci. Geomech. Abstr. 18, 221–228. http://dx.doi.org/10.1016/0148-9062(81)90976-1.

Paluszny, A., Matthäi, S.K., Hohmeyer, M., 2007. Hybrid finite element-finite volume discretization of complex geologic structures and a new simulation workflow demonstrated on fractured rocks. Geofluids 7, 186–208. http://dx.doi.org/10.1111/j.1468-8123.2007.00180.x.

Philip, Z.G., Jennings, J.W., Olson, J.E., Laubach, S.E., Holder, J., 2005. Modeling coupled fracture-matrix fluid flow in geomechanically simulated fracture networks. SPE Reserv. Eval. Eng. 8, 300–309. http://dx.doi.org/10.2118/77340-PA.

Pollard, D.D., Segall, P., 1987. Theoretical displacements and stresses near fractures in rock: with applications to faults, veins, dikes, and solution surfaces. In: Atkinson, B.K. (Ed.), Fracture Mechanics of Rock. Elsevier, London, 277–349. http://dx.doi.org/10.1016/B978-0-12-066266-1.50013-2.

Reif, D., Grasemann, B., Faber, R.H., 2011. Quantitative structural analysis using remote sensing data: Kurdistan, northeast Iraq. Am. Assoc. Pet. Geol. Bull. 95, 941–956. http://dx.doi.org/10.1306/11151010112.

Reith, D.F.H., 2015. Analysis of the Different Impacts Influencing the Value of the Fractal Dimension Regarding the Whitby Mudstone Formation (UK) & Jandaira Formation (Brazil). Delft University of Technology, Delft, Netherlands.

Rotevatn, A., Buckley, S.J., Howell, J.A., Fossen, H., 2009. Overlapping faults and their effect on fluid flow in different reservoir types: a LIDAR-based outcrop modeling and flow simulation study. Am. Assoc. Pet. Geol. Bull. 93, 407–427. http://dx.doi.org/10.1306/09300807092.

Sanderson, D.J., Nixon, C.W., 2015. The use of topology in fracture network characterization. J. Struct. Geol. 72, 55–66. http://dx.doi.org/10.1016/j.jsg.2015.01.005.

Scholz, C.H., 2011. Reply to comments of Jon Olson and Richard Schultz. J. Struct. Geol. 33, 1525–1526. http://dx.doi.org/10.1016/j.jsg.2011.07.006.

Shah, S., Møyner, O., Tene, M., Lie, K.A., Hajibeygi, H., 2016. The multiscale restriction smoothed basis method for fractured porous media (F-MsRSB). J. Comput. Phys. 318, 36–57. http://dx.doi.org/10.1016/j.jcp.2016.05.001.

Tao, Q., Ehlig-Economides, C.A., Ghassemi, A., 2009. Investigation of stress-dependent permeability in naturally fractured reservoirs using a fully coupled poroelastic displacement discontinuity model. In: Proceedings of SPE Annual Technical Conference and Exhibition, Society of Petroleum Engineers, New Orleans, Louisiana. doi:10.2118/124745-MS.

Tavani, S., Corradetti, A., Billi, A., 2016. High precision analysis of an embryonic extensional fault-related fold using 3D orthorectified virtual outcrops: the viewpoint importance in structural geology. J. Struct. Geol. 86, 200–210. http://dx.doi.org/10.1016/j.jsg.2016.03.009.

Tavani, S., Granado, P., Corradetti, A., Girundo, M., Iannace, A., Arbués, P., Muñoz, J.A., Mazzoli, S., 2014. Building a virtual outcrop, extracting geological information from it, and sharing the results in Google Earth via OpenPlot and Photoscan: an example from the Khaviz Anticline (Iran). Comput. Geosci. 63, 44–53. http://dx.doi.org/10.1016/j.cageo.2013.10.013.

Ullman, S., 1979. The interpretation of structure from motion. Proc. R. Soc. B Biol. Sci. 203, 405–426. http://dx.doi.org/10.1098/rspb.1979.0006.

Vasuki, Y., Holden, E.-J., Kovesi, P., Micklethwaite, S., 2014. Semi-automatic mapping of geological structures using UAV-based photogrammetric data: an image analysis approach. Comput. Geosci. 69, 22–32. http://dx.doi.org/10.1016/j.cageo.2014.04.012.

Vermilye, J.M., Scholz, C.H., 1995. Relation between vein length and aperture. J. Struct. Geol. 17, 423–434. http://dx.doi.org/10.1016/0191-8141(94)00058-8.

Vollgger, S.A., Cruden, A.R., 2016. Mapping folds and fractures in basement and cover rocks using UAV photogrammetry, Cape Liptrap and Cape Paterson, Victoria, Australia. J. Struct. Geol. 85, 168–187. http://dx.doi.org/10.1016/j.jsg.2016.02.012.

Wilson, C.E., Aydin, A., Karimi-Fard, M., Durlofsky, L.J., Amir, S., Brodsky, E.E., Kreylos, O., Kellogg, L.H., 2011. From outcrop to flow simulation: constructing discrete fracture models from a LIDAR survey. Am. Assoc. Pet. Geol. Bull. 95, 1883–1905. http://dx.doi.org/10.1306/03241108148.

Wu, H.Q., Pollard, D.D., 2002. Imaging 3-D fracture networks around boreholes. Am. Assoc. Pet. Geol. Bull. 86, 593–604. http://dx.doi.org/10.1306/61EEDB52-173E-11D7-8645000102C1865D.

Zhang, L., Einstein, H.H., 1998. Estimating the mean trace length of rock discontinuities. Rock. Mech. Rock Eng. 31, 217–235. http://dx.doi.org/10.1007/s006030050022.

Zoback, M.D., 2007. Reservoir Geomechanics, Reservoir Geomechanics. Cambridge University Press, Cambridge. http://dx.doi.org/10.1017/CBO9780511586477.